Available online at www.sciencedirect.com
ScienceDirect
Proceedings of the Combustion Institute 32 (2009) 777–784
Proceedings of the Combustion Institute
www.elsevier.com/locate/proci

Computational and experimental investigation of the interaction of soot and NO in coflow diffusion flames

B.C. Connelly [a], M.B. Long [a], M.D. Smooke [a,*], R.J. Hall [b], M.B. Colket [b]

[a] Department of Mechanical Engineering, Yale University, 15 Prospect Street, New Haven, CT 06520-8284, USA
[b] United Technologies Research Center, East Hartford, CT 06108, USA

Abstract

A combined computational and experimental investigation that examines the relationship of soot formation and NO in coflow ethylene air diffusion flames is presented. While both NO and soot formation are often studied independently, there is a need to understand their coupled relationship as a function of system parameters such as fuel type, temperature and pressure. The temperature decrease due to radiative losses in systems in which significant soot is produced can affect flame length and other temperature-dependent processes such as the formation of NO. The results of a computational model that includes a sectional representation for soot formation with a radiation model are compared against laser-induced fluorescence measurements of NO. The sooting characteristics of these flames have been studied previously. Experimentally, a laser near 225.8 nm is used to excite the $\gamma(0,0)$ band in NO. Spectrally resolved fluorescence emission is imaged radially, for the (0,0), (0,1), (0,2), (0,3), and (0,4) vibrational bands, at varying axial heights to create a two-dimensional image of NO fluorescence. A reverse quenching correction is applied to the computational results to determine an expected fluorescence signal for comparison with experimental results. Modeling results confirm that Fenimore NO is the dominant mechanism for NO production and suggest that for lightly sooting flames (peak soot volume fraction < 0.5 ppm), soot reduces only the Zeldovich NO formation (by a factor of two). For flames with increased soot levels (peak soot volume fraction ~ 4 ppm), the model indicates not only that Zeldovich NO decreases by a factor of 2.5 through radiation loss, but that non-Zeldovich NO is reduced in the top center of the flame by about 30% through the oxidation of soot.

Keywords: Diffusion flame; NO; Soot; Computation; Diagnostics

1. Introduction

The push for higher combustion efficiency in propulsion applications that has dominated much of combustion research in the past few decades is being replaced by a move towards cleaner combustion. Increased environmental consciousness and stricter air quality legislation is now driving research in the area of pollutant formation and control to the point where it is becoming economically indispensable to the export of combustion-related technologies and products worldwide.

As emissions legislation becomes more restrictive, a detailed understanding of pollutant

* Corresponding author. Fax: +1 203 432 6775.
E-mail address: mitchell.smooke@yale.edu (M.D. Smooke).

1540-7489/$ - see front matter © 2009 The Combustion Institute. Published by Elsevier Inc. All rights reserved.
doi:10.1016/j.proci.2008.06.182

formation in flames will become even more critical for the design of pollutant abatement strategies and for the preservation of the competitiveness of combustion-related industries. In particular, it is clear that there will be continuing pressure to lower both NO_x emission indices and soot volume fractions in practical combustion devices. This is in response to the toxicological effects that small particles can have on the body's cardio-pulmonary system [1,2] and to the impact, for example, that soot can have on thermal radiation loads in combustors and on turbine blades. Moreover, soot emissions can enhance contrail formation [3] and such "man made" clouds may have an impact ultimately on the Earth's climate [4,5].

The temperature decrease due to radiative losses in systems in which significant soot is produced can affect flame length and other temperature-dependent processes such as the formation of NO. While both NO and soot formation are often studied independently, there is a desire to understand their coupled relationship as a function of system parameters such as fuel type, temperature and pressure. In this manuscript we combine a computational and experimental investigation to examine the interrelationship of soot formation and NO in coflow ethylene air diffusion flames. This analysis is performed excluding any direct NO-soot reactions. Specifically, the results of a computational model that includes detailed chemistry for gas-phase processes and a sectional representation for soot formation, along with optically-thin radiation, are compared against laser-induced fluorescence (LIF) measurements of NO. The detailed information on the temperature and species concentrations in the computed flame are combined with an NO quenching model to predict the LIF signal from NO that is measured experimentally. Once the modeling technique is qualitatively validated against the data sets, computations are performed to assess the impact of soot (and related radiation) on the NO field. In the next section the soot formation model is outlined. This is followed by the experimental procedure and the solution method. The paper concludes with a discussion of the results.

2. Soot formation model

The soot formation model is described in detail in [6]. The inception model is based on the sequence of growing naphthalenyl to pyrenyl through sequential acetylene addition, H-atom elimination, H-atom abstraction, and acetylene addition followed by ring closure. Overall, the reaction can be written $C_{10}H_7 + 3C_2H_2 \Leftrightarrow C_{16}H_9 + 2H + H_2$. This sequence is assumed to continue to form yet larger polycyclic aromatic hydrocarbons (PAH) structures with the overall balance of $C_{10}H_7 + 3nC_2H_2 \Leftrightarrow C_{10+6n}H_{7+2n} + 2nH + nH_2$. Quasi steady-state concentrations of intermediate PAH are assumed, leading to steady-state expressions for the formation rates of these high molecular weight condensed PAH. The computed soot results are relatively independent of the number, n, assigned to the inception species and equal to 21 in this work.

The surface growth model used in the simulations is based on the premixed flame data of Harris and Weiner [7] where we assumed an activation energy of $E_s = 31.8$ kcal/mole [8] and where we multiplied the nominal Arrhenius factor by two (see also [6,9,10]). Surface growth is first order in acetylene concentration in this model. Oxidation of soot by O_2 and OH is treated as described in [9,10]. In the assumed free-molecule, large Knudsen number regime, surface growth and oxidation rates are proportional to particle surface area.

The growth of soot particles is modeled as an aerosol dynamics problem, using the well-known sectional particle size representation for spheres [11]. The application of this approach to soot modeling is described in [6,9,10,12,13]. The contributions from the inception processes are incorporated as a source term in the dynamical equation for the first sectional bin, whose lower mass boundary is set equal to the mass of the assumed inception species. Calculated results were not significantly sensitive to the number of sections assumed, with 20 sections used in all the calculations reported here.

Radiative losses can have a significant influence on NO levels in flames where soot is present compared to nonsooting systems [14–16]. For the small flames computed in this study with low soot volume fractions, the power radiated from soot and gas bands (CO_2, H_2O, and CO) can be computed in the optically-thin limit using the expressions in [17]. While temperature changes associated with radiation are not large, the great sensitivity of soot growth (and NO) to temperatures makes the incorporation of radiation effects important. In higher soot loading flames, the optically-thin model tends to overestimate the radiation losses and, in principle, some re-absorption of thermal emissions can occur, particularly on or near the centerline, which receives emissions from surrounding regions of the flame. This optical thickness effect reduces the net rate of thermal radiation energy loss and locally raises the temperature. Overall, however, the soot formation model has given quite satisfactory agreement with measured peak soot volume fractions as well as soot spatial distributions and temperatures in the flames studied (see, e.g., [6,9,10,13]).

3. Experimental procedure

Atmospheric pressure, axisymmetric, coflowing, nonpremixed laminar diffusion flames are generated with a burner in which the fuel flows from an uncooled 4.0 mm inner diameter vertical steel tube (wall thickness 0.38 mm, parabolic flow) into a concentric, 74 mm diameter air coflow (plug flow). The details of the burner used are kept consistent with previous studies [6,13]. The flame is lifted above the burner surface, preventing heat transfer from the flame to the burner. The fuel (ethylene) is diluted with varying levels of inert (nitrogen) to control the soot loading within the flame. Two flames with different fuel dilutions are examined: a 40% ethylene/60% nitrogen flame and an 80% ethylene/20% nitrogen flame.

The third harmonic of a Nd:YAG laser pumps a dye laser containing coumarin 450 dye. The 452 nm dye laser output is doubled using a BBO crystal, producing an ultraviolet (UV) beam near 225.8 nm, which is used to excite transitions in the $A^2\Sigma^+ - X^2\Pi$ (0,0) band of NO. An excitation scan over a spectral range from 225.5 to 226.5 nm was matched with the various spectral features of NO [18]. The $Q_1(18)$ transition (44275.684 cm^{-1}) was selected for this work. This transition is reasonably well separated from neighboring transitions and has significant population from room temperature to the flame temperatures investigated. Aside from soot interferences, which possess a broadband spectrum, no significant spectral interferences were encountered in the laminar flames investigated [19].

There are two burners in the optical path. A dichroic mirror steers the UV beam down the measurement path, and removes the majority of the laser energy at 452 nm. A beamsplitter steers ~30% of the energy in the UV beam 4 cm above a premixed reference burner. NO fluorescence from the center of a lean propane flame is imaged with a quartz lens onto a 1 mm slit, through an interference filter at 260 nm (12.5 nm bandwidth) centered on the (0,3) vibrational band. The signal is detected with a PMT (Hamamatsu R166UH) connected to a digital oscilloscope. This signal is used to provide a fluorescence normalization that accounts for variations in laser energy and ensures that the laser wavelength does not shift off of the peak of the NO transition being pumped. The UV beam remaining after the beamsplitter (~60 μJ per pulse) is directed across the target diffusion flame burner. Because the remaining energy from the 452 nm beam (~100 μJ) causes interference in sooty regions of the flame, the two wavelengths are separated using a quartz prism. The remaining UV beam still produces unavoidable soot interferences. A 25 cm focal length quartz lens focuses the UV beam across the diffusion flame. To ensure that the fluorescence is in the linear regime, the measurements are made 10 cm before the focus of the UV beam, resulting in a beam diameter of 0.5 mm in the measurement region. While this beam diameter sacrifices some spatial resolution in the axial direction, features of the NO LIF in the axial direction are observed (both experimentally and computationally) to be larger than the beam diameter. Finer structures in the NO LIF occur in the radial direction, where the spatial resolution is superior (0.13 mm, using Nyquist sampling criteria). The laser energies at 225.8 nm and at 452 nm are monitored using two pyroelectric energy meters (LaserProbe RjP-734) connected to a second oscilloscope.

NO fluorescence in the diffusion flame is imaged onto a 500-μm entrance slit of a spectrograph (SPEX 270M) using a UV camera lens (UV-Nikkor 105 mm, *f*/4.5) and a 10 cm focal length quartz lens. When taking data in sooty regions within the flame, a colored glass filter (Corning 7-54) is placed between the two collection lenses to suppress the Rayleigh scattering by the soot, which would otherwise saturate the detector. Spectral resolution is sacrificed by using a relatively wide entrance slit to compensate better for wandering of the beam through the measurement volume. The fluorescence is dispersed with a 300 groove/mm grating (250 nm blaze angle) and imaged with an intensified CCD detector (a gated Gen II intensifier optically coupled to a Princeton Instruments TE/CCD-512 CCD). The CCD image contains information in one spatial and one spectral dimension. Spatially, a line extending from the centerline to 10 mm in the radial direction is imaged, and spectrally the region from 220 to 300 nm is recorded. The spectral region includes Rayleigh scattering (overlapped with the (0,0) fluorescence) as well as the (0,1), (0,2), (0,3), and (0,4) vibrational fluorescence bands. The fluorescence signal is integrated on the detector for 12.8 s (128 laser pulses), chosen to correspond to event sampling on the oscilloscopes. The experiment is controlled through a computer, which records synchronized data from the CCD camera and the digital oscilloscopes. Data are acquired both with the laser tuned to the $Q_1(18)$ peak, and with the laser tuned off-resonance (near 225.65 nm), to provide a correction for soot interferences.

The final fluorescence image is obtained by summing the fluorescence intensity over a 7.5 nm spectral region centered on the (0,2) transition [20]. No significant difference is noted when the detection band is centered on the (0,1) or on the (0,3) transition. A two-dimensional image of the NO fluorescence distribution is created by tiling together a series of spatial/spectral images recorded at 0.5-mm intervals from 2 to 100 mm above the burner. Each image is corrected for detector and soot incandescence backgrounds, normalized by the reference fluorescence signal recorded by the PMT, and corrected for

nonuniform detector gain and optical throughput. This latter "response" correction is obtained by imaging the fluorescence from a calibration gas (45.2 ppm NO in N_2 mixed with 3% O_2, by volume), which results in a uniform NO concentration field in the imaged region that also provides a room temperature signal calibration. The final corrected fluorescence image has a signal-to-noise ratio of ~50 in the downstream region, where the NO signal was highest, and a pixel volume of $0.1 \times 0.5 \times 0.5\ mm^3$.

For fluorescence in the linear regime, the scattered intensity is dependent on a number of variables, including the total number density, the Boltzmann population fraction, and the total collisional quenching rate. For NO, the quenching term is particularly important, and varies significantly with temperature and with quenching partners. Fortunately, a good deal of information is available on NO quenching, both in the form of experimental measurements and models [20–22]. Due to the soot within the target flames, it is difficult to characterize the flame temperature and major species. Consequently, we cannot apply the quenching and Boltzmann corrections to the measured fluorescence signal. Instead, we have applied a reverse quenching correction [23,24] to the calculated flame to determine an expected fluorescence signal for comparison with the experimental results [25]. The model of Settersten et al. [22] is used to account for the temperature-dependent quenching by CO_2, H_2O, O_2, N_2, and CO. Both the measured fluorescence and the calculated fluorescence are normalized using the calibration gas to provide a quantitative comparison of fluorescence signals.

4. Computational methodology

We consider an unconfined, axisymmetric, laminar diffusion flame in which a cylindrical fuel stream is surrounded by a coflowing oxidizer jet. The full set of elliptic two-dimensional governing equations – mass, momentum, species, and energy – are solved in a vorticity–velocity formulation [26], using a flame sheet starting estimate [27], and the differential operators are discretized on an adaptively refined mesh. The resulting nonlinear equations are solved by a combination of time integration and Newton's method with several theoretical estimates [28] that help determine when a new Jacobian should be reformed. The Newton equations are solved by a preconditioned Bi-CGSTAB iteration with a Gauss–Seidel preconditioner. Pseudo time-stepping is used to ease convergence difficulties associated with the starting estimate. The size of the time-steps is chosen by monitoring the local truncation error of the time discretization process (see also [29]). The binary diffusion coefficients, the viscosity, the thermal conductivity of the mixture, the chemical production rates as well as the thermodynamic quantities were evaluated using vectorized and highly optimized transport and chemistry libraries [30].

5. Results

In this section we present the results of a series of computations and LIF experiments in which NO formation is examined in sooting, ethylene–air, coflow diffusion flames where the radiation field is computed with an optically-thin model. We consider flames with 40% and 80% (mole fraction) ethylene diluted with nitrogen. The computations employ the ethylene mechanism in [31] coupled with the nitrogen chemistry submechanism in GRI 2.11 [32]. We decided on the GRI 2.11 submechanism as opposed to the newer one in GRI 3.0 [33] as the latter significantly over-predicts (by a factor of 2.5) NO downstream in our coflow flames [34]. The result is a reaction network containing 84 chemical species with 578 reactions. The velocity profile of the ethylene fuel tube was parabolic with an average velocity of 35 cm/s. The air coflow was a plug flow profile with a velocity of 35 cm/s. The gases emerged from the burner at 298 K. All computations were performed on a 1.4 GHz AMD Dual Opteron processor.

NO can be formed in hydrocarbon flames by several different mechanisms (see e.g., [35–37]). The Zel'dovich or thermal NO mechanism [38] as extended by Bowman and Seery [39] is initiated by the reaction of N_2 with O. This well-known 3-step reaction sequence is the dominant NO forming route at temperatures above 1850 K. A second path consists of reactions involving N_2O, which form NO. NO formed via this mechanism increases at higher pressures. A third mechanism responsible for NO formation is (prompt) "Fenimore NO." The main steps influencing this reaction sequence are $N_2 + CH = HCN + N$, $N_2 + CH_2 = HCN + NH$ and other reactions involving N_2 and hydrocarbon radicals. Lastly, NO can be formed via the $H + N_2 = NNH$, followed by $O + NNH = NO + NH$ sequence. GRI 2.11 includes these latter reactions but not with the higher rates suggested by Bozzelli and Dean [35]. The NO formation rates of each of these reaction sequences can be enhanced through super-equilibrium levels of O-atoms and other radical species in the flame front.

To assess the Zel'dovich/non-Zel'dovich NO distribution, additional computations were carried out with only the extended Zel'dovich submechanism appended to the hydrocarbon mechanism. We note that in prior work in which we examined the origins of NO in atmospheric pressure coflow methane–air diffusion flames [24], we found that the N_2O and NNH submech-

anisms contributed minimally to overall NO levels. As a result, we will not examine the impact of these two submechanisms specifically on the overall NO levels but will assign all NO above the Zel'dovich mole fraction levels as non-Zel'dovich NO (in practice, this is almost totally Fenimore NO).

In Fig. 1 we illustrate NO mole fractions for the 40% ethylene/60% nitrogen flame computed with the extended Zel'dovich submechanism. When soot is included in the model (Fig. 1a), we obtain a maximum soot volume fraction of 1.3 ppm with a peak NO of 22 ppm. The peak temperature is 2006 K. When the computation was performed without the inclusion of soot (Fig. 1b), the peak temperature increased to 2055 K and the NO increased to 40 ppm. From the isopleths in the figure, we note that the region of NO above 20 ppm is larger in extent in the nonsooting flame compared to that of the sooting flame.

The NO mole fractions for the 40% flame computed with the complete NO mechanism are also illustrated in Fig. 1. When soot is included in the computation (Fig. 1c), the peak NO increases to 140 ppm. Most of the 118 ppm increase compared to the Zel'dovich computation is due to Fenimore NO. If soot is removed from the computation (Fig. 1d), the NO increases to 160 ppm and again the 120 ppm increase over the Zel'dovich computation is due mostly to Fenimore NO. The spatial distribution of the NO is generally quite similar for these two computations. For reference purposes, we point out that the sooting 40% flame had an overall powerloss of 16.1 W of the total 102 W generated.

As mentioned earlier, due to soot formation within the flame, we cannot easily characterize the flame temperature and major species. Hence, the quenching and Boltzmann corrections cannot be applied to the measured fluorescence signal. Instead, we have applied a reverse quenching and Boltzmann correction to the computed flame profiles to determine an expected fluorescence signal. This simulated signal is calibrated by an expected fluorescence signal from a gas of the same composition as in the experiment, to provide a quantitative comparison. In Fig. 2 we plot the computed and measured NO fluorescence signals as a function of the spatial variables for the 40% flame. Also plotted is the soot volume fraction measured using laser-induced incandescence (LII). For details on the LII experiment for both the 40% and 80% flames, as well as comparison to numerically computed soot volume fractions, see [13]. The results show good qualitative agreement overall; for example, the fairly constant signal level in the regions above the flames, as well as the lower signal inside the flame/sooty areas, are captured. We note that the computed fluorescence signal under-predicts the measured fluorescence signal by approximately 30%.

We next performed computations for the 80% ethylene/20% nitrogen flame. In Fig. 3 NO mole fractions are plotted for computations with only the Zel'dovich submechanism. When soot is included (Fig. 3a), we obtain a maximum soot volume fraction of 4.4 ppm and a total of 40 ppm of NO. The peak temperature of 2083 K occurred in the wings of the flame while the peak centerline temperature was 1736 K. When the computation is performed without soot (Fig. 3b), the NO increases to 110 ppm and the peak temperature of 2107 K occurs on the centerline. Once again the spatial extent of the high NO levels is significantly larger for the computation in which soot is not included though the higher region of NO in the sooting flame extends further down the wings of the flame.

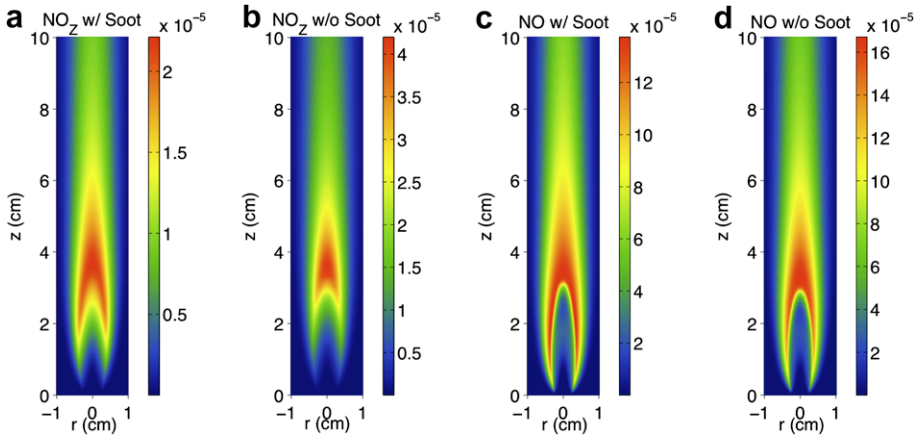

Fig. 1. Computational NO mole fractions for the 40% ethylene/60% nitrogen flame generated with: (a) the extended Zel'dovich submechanism, including soot; (b) the extended Zel'dovich submechanism, neglecting soot; (c) the complete NO_x submechanism, including soot; (d) the complete NO_x submechanism, neglecting soot.

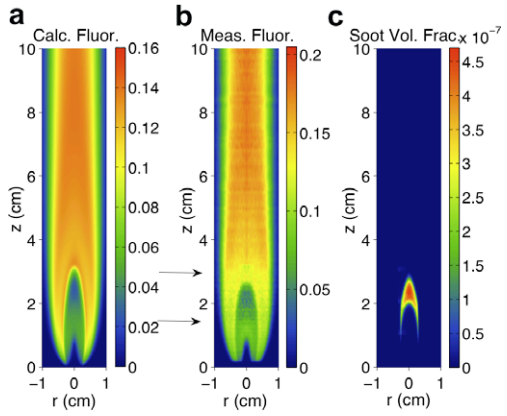

Fig. 2. Comparison of the computed (a) and measured (b) fluorescence signal from NO for the 40% ethylene/60% nitrogen coflow flame. The fluorescence signal has been normalized with respect to a calibration gas for both the computed and measured plots. Experimentally, a colored glass filter was added to the input optics in the region between the arrows to minimize soot interferences. The soot volume fraction (c) is measured using LII.

The 80% flame was then rerun with the complete NO mechanism. In the sooting case (Fig. 3c), the peak NO increased to 170 ppm. Most of the 130 ppm increase was due to Fenimore NO. If soot was removed from this computation (Fig. 3d), the NO increased to 240 ppm and again the 130 ppm increase over the Zel'dovich submechanism computation was due mostly to Fenimore NO. What is striking in these two results is the change in the spatial orientation of the NO with or without soot. For the sooting flame, the highest NO extends in a narrow region in the wings of the flame. For the case when soot was neglected, the NO extends much further downstream with somewhat smaller extent in the wings. The 80% sooting flame had an overall powerloss of 53.3 W of the total 203 W generated.

In Fig. 4 we plot the computed and measured NO fluorescence signals and the measured soot volume fraction as a function of the spatial variables for the 80% flame. As with the 40% flame, there is qualitative agreement between the computed and measured fluorescence signals, with the computed signal approximately 30% lower overall than the measured signal.

A clear contrast exists in the NO and temperature levels between the two 80% flames with the full NO mechanism. In the solution with soot, the NO levels and temperature are noticeably depressed along the centerline relative to the off-centerline conditions in the "wings" of the flame. Such results not only contrast with the 40% flame solutions, but also for the 80% flame solutions without any soot or its radiation. In the latter case, elimination of soot removes an important loss of energy from the flame and centerline temperatures nearly recover and peak NO levels occur on the centerline.

Perhaps the most unusual feature of Fig. 3c is the depression of NO concentration in the upper centerline region. (A similar depression did not exist for the 40% flame depicted in Fig. 1c.) The NO concentration in this upper centerline region is ~120 ppm vs. the 170 ppm in the side wings of the flame. Given that the Zel'dovich mechanism gives a large broad contour in this region, it can be deduced that the Fenimore mechanism is suppressed in this region. To examine whether this is soot-related, we have plotted the difference between panels in Fig. 3c and a, as well as the difference between panels 3d and 3b. These differences are shown in Fig. 5a and b, respectively. These figures provide a qualitative assessment on the change in Fenimore NO with and without soot. The depression in the upper centerline region for the flame with soot is quite significant. Similar

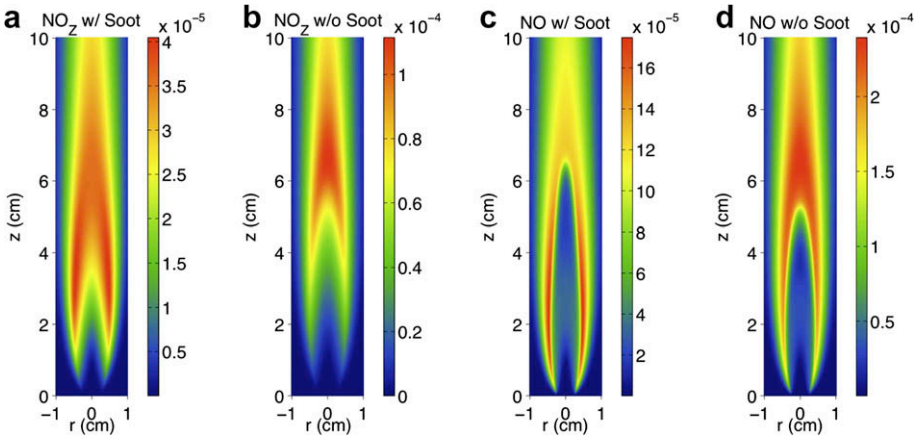

Fig. 3. Same as Fig. 1 for the 80% ethylene/20% nitrogen flame.

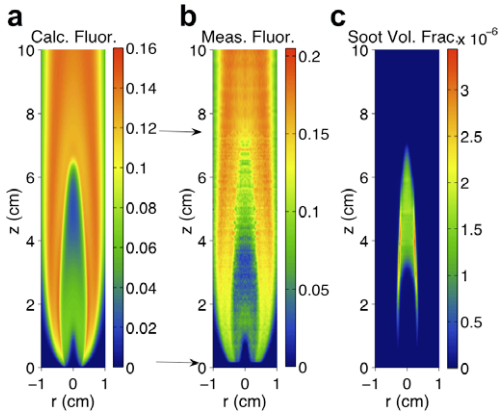

Fig. 4. Same as Fig. 2 for the 80% ethylene/20% nitrogen flame.

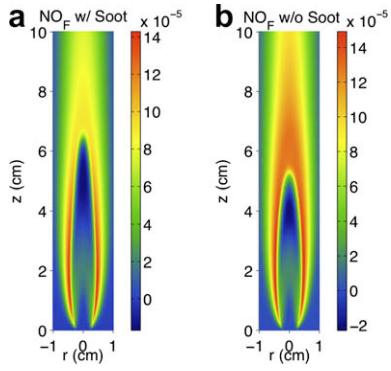

Fig. 5. Computational NO mole fractions for the 80% ethylene/20% nitrogen flame, plotted as differences between the complete NO_x submechanism and the extended Zel'dovich submechansim to approximate Fenimore NO: (a) the difference between panels in Fig. 3c and a, including soot; (b) the difference between panels in Fig. 3d and b, neglecting soot.

plots for the 40% flame do not exhibit this strong effect.

As Fenimore NO is weakly dependent on temperature, the results in Fig. 5 are clearly due to the presence of soot in the flame. To help appreciate the effect that soot has on NO formation, it is worthwhile to recognize that in premixed flames with soot levels of $f_v = 4$ ppm and $\varphi = 2$, about 1/4 of the total fuel carbon is converted to soot. We propose that some of the difference in the upper centerline regions between Fig. 5a and b may be due simply to fewer hydrocarbon fuel fragments available to form CH or CH_2 as the soot oxidizes directly to CO and H after attack by OH. In addition, soot oxidation along the centerline slightly delays the completion of combustion (relative to that by gas-phase species). The slower oxidation rate reduces local super-equilibrium radical levels that promote NO formation and reduce the driving force for diffusion of molecular oxygen to the centerline of the flame, reducing NO production rates and lengthening the flame in the process. The relative importance of each of these phenomena will take additional computation and analysis.

It is well established that, as we have found, many practical systems exhibit a reverse trend in NO and sooting levels. Typically, it is assumed that this is at least partially a result of local conditions, with more soot formed in a local fuel-rich environment and more NO formed in the near stoichiometric regions. The present results from both the 40% and the 80% flames imply a complication of this interdependency, with mitigation of NO production rates directly due to the formation of soot and local radiation losses. For the 80% flames the affects are so significant that they alter the NO profile shape in the flame, shifting the peak NO from the centerline to the wings of the flame.

6. Conclusions

We have combined LIF measurements and computations using a detailed chemistry coflow diffusion flame model with a sectional aerosol model to examine the effects of soot formation on NO levels in ethylene–air diffusion flames. Results indicate that while the dominant route to NO in these flames is due to non-Zel'dovich NO (primarily prompt), Zel'dovich NO is more pronounced in the 80% ethylene flame compared to the 40% ethylene flame. Moreover, when the soot field is removed from the model and the solution recomputed with a new radiation field, Zel'dovich NO accounts for nearly 46% of total NO in the 80% flame and 25% of total NO for the 40% flame which are significantly larger than 24% and 16%, respectively, for the sooting flames. Furthermore, the results indicate that not only does soot and accompanying radiation loss (virtually all from Zel'dovich NO) reduce the levels of NO throughout the flame, but for heavier sooting flames, the shape of the NO profile shifts, with NO levels in the wings noticeably higher than centerline levels. These results imply a coupled relationship between soot levels and NO that require a careful application of diagnostics and computation to help elucidate our understanding of these flames.

Acknowledgments

The authors acknowledge support for this work from the DOE Office of Basic Energy Sciences (Dr. Frank Tully, contract monitor), the National Science Foundation (Dr. Linda Blevins, contract monitor), and NASA (Dr. Dennis Stocker, contract monitor) under contracts DE-FG02-88ER13966, CTS-0328296, and NNC04AA03A,

respectively. In addition, we gratefully acknowledges the Strategic Environmental Research and Development Program (SERDP) under a contract coordinated by Dr. Mel Roquemore of the Air Force Research Laboratories (Wright Patterson AFB).

References

[1] J. Schwartz, *Environ. Res.* 62 (1993) 7–13.
[2] D.W. Dockery, J.H. Ware, B.G. Ferris, F.E. Speizer, N.R. Cook, S.M. Herman, *J. Air Pollut. Control Assoc.* 32 (1982) 937–942.
[3] U. Schumann, J. Strom, R. Busen, et al., *J. Geophys. Res.: Atmos.* 101 (1996) 6853–6869.
[4] S. Menon, J. Hansen, L. Nazarenko, Y.F. Luo, *Science* 297 (2002) 2250–2253.
[5] J.E. Penner, D.H. Lister, D.J. Griggs, D.J. Dokken, M. McFarland, *Aviation and the Global Atmosphere*, A Special Report of IPCC Working Groups I and III. Cambridge University Press, 1999.
[6] M.D. Smooke, R.J. Hall, M.B. Colket, et al., *Combust. Theory Model.* 8 (2004) 593–606.
[7] S.J. Harris, A.M. Weiner, *Combust. Sci. Technol.* 31 (1983) 155–167.
[8] H.S. Hura, I. Glassman, *Proc. Combust. Inst.* 22 (1988) 371–378.
[9] M.D. Smooke, C.S. McEnally, L.D. Pfefferle, R.J. Hall, M.B. Colket, *Combust. Flame* 117 (1999) 117–139.
[10] C.S. McEnally, A. Schaffer, M.B. Long, et al., *Proc. Combust. Inst.* 27 (1998) 1497–1505.
[11] F. Gelbard, J.H. Seinfeld, *J. Colloid Interf. Sci.* 78 (1980) 485–501.
[12] R.J. Hall, M.D. Smooke, M.B. Colket, in: R.F. Sawyer, F.L. Dryer (Eds.), *Physical and Chemical Aspects of Combustion: A Tribute to Irvin Glassman*, Gordon and Breach, 1997.
[13] M.D. Smooke, M.B. Long, B.C. Connelly, M.B. Colket, R.J. Hall, *Combust. Flame* 143 (2005) 613–628.
[14] X.L. Zhu, J.P. Gore, *Combust. Flame* 141 (2005) 118–130.
[15] S.V. Naik, N.M. Laurendeau, J.A. Cooke, M.D. Smooke, *Combust. Flame* 134 (2003) 425–431.
[16] S.V. Naik, N.M. Laurendeau, J.A. Cooke, M.D. Smooke, *Combust. Sci. Technol.* 175 (2003) 1165–1177.
[17] R.J. Hall, *J. Quant. Spectrosc. Radiat. Trans.* 51 (1994) 635–644.
[18] R. Engleman Jr., P.E. Rouse, H.M. Peek, V.D. Baiamonte, *Beta and Gamma Systems of Nitric Oxide*, Los Alamos Scientific Laboratory, Los Alamos, NM, 1970.
[19] C.D. Carter, R.S. Barlow, *Opt. Lett.* 19 (1994) 299–301.
[20] M.C. Drake, J.W. Ratcliffe, *J. Chem. Phys.* 98 (1993) 3850–3865.
[21] P.H. Paul, J.A. Gray, J.L. Durant, J.W. Thoman, *Appl. Phys. B: Photophys. Laser Chem.* 57 (1993) 249–259.
[22] T.B. Settersten, B.D. Patterson, J.A. Gray, *J. Chem. Phys.* 124 (2006).
[23] V. Sick, F. Hildenbrand, P. Lindstedt, *Proc. Combust. Inst.* 27 (1998) 1401–1409.
[24] M.D. Smooke, A. Ern, M.A. Tanoff, et al., *Proc. Combust. Inst.* 26 (1996) 2161.
[25] J.B. Bell, M.S. Day, J.F. Grcar, et al., *Proc. Combust. Inst.* 29 (2003) 2195–2202.
[26] A. Ern, M.D. Smooke, *J. Comput. Phys.* 105 (1993) 58–71.
[27] D.E. Keyes, M.D. Smooke, *J. Comput. Phys.* 73 (1987) 267–288.
[28] M.D. Smooke, *J. Optimiz. Theory Appl.* 39 (1983) 489–511.
[29] M.D. Smooke, R.E. Mitchell, D.E. Keyes, *Combust. Sci. Technol.* 67 (1989) 85–122.
[30] V. Giovangigli, N. Darabiha, *Vector Computers and Complex Chemistry Combustion, in: Proceedings of the Conference of Mathematical Modeling in Combustion*, Lyon, France, 1987.
[31] C.J. Sun, C.J. Sung, H. Wang, C.K. Law, *Combust. Flame* 107 (1996) 321–335.
[32] C.T. Bowman, R.K. Hanson, D.F. Davidson, et al., GRI-Mech version 2.11, 1995, available at http://www.me.berkeley.edu/gri_mech/.
[33] G.P. Smith, D.M. Golden, M. Frenklach, et al., GRI-Mech version 3.0, available at http://www.me.berkeley.edu/gri_mech/.
[34] B.A.V. Bennett, M.D. Smooke, R.J. Osborne, R.W. Pitz, *Combust. Theory Model.* 12 (2008) 497–527.
[35] J.W. Bozzelli, A.M. Dean, *Int. J. Chem. Kinet.* 27 (1995) 1097–1109.
[36] M.C. Drake, R.J. Blint, *Combust. Sci. Technol.* 75 (1991) 261–285.
[37] J.A. Miller, C.T. Bowman, *Prog. Energy Combust. Sci.* 15 (1989) 287–338.
[38] Y.B. Zel'dovich, *Acta Physecochem USSR* 21 (1946) 557.
[39] C.T. Bowman, D.V. Seery, *Emissions from Continuous Combustion Systems*, Plenum Press, New York, 1972.